
Article:
Yang, B., Xu, H., Liu, W. orcid.org/0000-0003-2968-2888 et al. (2 more authors) (2018) Realistic Lower Bound on Elevation Estimation for Tomographic SAR. IEEE Journal of Selected Topics in Applied Earth Observations and Remote Sensing, 11 (7). pp. 2429-2439. ISSN 1939-1404

https://doi.org/10.1109/JSTARS.2018.2834950

Realistic Lower Bound on Elevation Estimation for Tomographic SAR

Bo Yang, Huaping Xu, *Member, IEEE,* Wei Liu, *Senior Member, IEEE*, Yanan You, and Xiaozhen Xie

***Abstract*—The noise in a tomographic synthetic aperture radar (Tomo-SAR) model is normally assumed to be independent and identically distributed (i.i.d.) Gaussian. In this work, the correlated Tomo-SAR model is introduced by studying the effect of random residual phase and correlated additive Gaussian noise, and a realistic and general hybrid Cramér-Rao bound (CRB) on elevation estimation is derived for such a model. Then, a simplified calculation of the HCRB is proposed when the bound of elevation is the main focus. Computer simulations are performed to analyze the proposed HCRB for elevation estimation. The results obtained from estimators based on compressive sensing (CS) and distributed compressive sensing (DCS) show that the proposed HCRB can provide a more realistic bound than the CRB derived with the white additive noise and perfect phase compensation assumption. This is also validated through processing results on real data acquired by TerraSAR-X/Tandem-X sensors.**

***Index Terms*—Synthetic aperture radar (SAR), SAR tomography (Tomo-SAR), Cramér-Rao bound (CRB), hybrid Cramér-Rao bound (HCRB), correlated noise, elevation accuracy.**

I. Introduction

TOMOGRAPHIC synthetic aperture radar (Tomo-SAR) is an extension of SAR interferometry (InSAR), where multiple views are utilized to map the scattering power at different heights, thus enabling 3-D imaging of the scenes [1]. Since it first demonstrated the resolution capability along the elevation direction by an airborne system [2], Tomo-SAR has attracted great interest and much progress has been made in the field of spaceborne multibaseline InSAR, especially for scenes with steep topography or high spatial density. A 2-D SAR image pixel can be considered as a projection of the 3-D scene scattering along the elevation direction onto the 2-D azimuth-range plane. Based on this principle, Fornaro et al. [3]–[5] first validated the capability based on spaceborne data and formulated the layover problem as a linear spectral estimation of the amplitude, phase and elevation parameters of the targets.

Based on the Tomo-SAR signal model, various estimators have been proposed for 3-D reconstruction with multipass SAR data over the same scene, such as beamforming, SVD-based methods, nonlinear least square (NLS), and their combined versions and variations (see [3], [4], [6], [7]). For spaceborne Tomo-SAR, estimators based on compressive sensing (CS) have been proposed to obtain a significantly improved elevation resolution [6]–[13]. However, for a small number of acquisitions, with unevenly sampled space and limited span of baselines, the performance of CS-based methods is not satisfactory for single stack elevation reconstruction. The neighborhood-based approach, distributed compressive sensing (DCS) or multilooking approach to compressive sensing (MCS), can mitigate the undersampling effect effectively and improve the performance further [14], [15]. In essence, the same supports of common components for neighboring azimuth-range pixels or multiple channels are exploited to reduce acquisition cost and help improve the elevation accuracy in [14]–[17].

It is important to analyze and evaluate the performance of an estimator before it is employed in practice. The theoretical lower bounds (see [18]–[28])[1], such as Cramér-Rao bound (CRB) and hybrid Cramér-Rao bound (HCRB), play an important role in predicting the performance of estimators, analyzing the system parameters and guiding their design. Zhu et al. derived the CRB of the single stack Tomo-SAR model in [8], following which Liang et al. obtained the CRB of multiple channels for the joint Tomo-SAR model [16]. Both works are based on the assumption that the overall noise containing both background clutters and thermal noise in a given pixel is independent among deramped SAR images, so that the CRB of unknown parameters can be derived using the results of [29] and [30]. Considering that clutters in the referred pixel between different SAR images are actually correlated in most cases, the HCRB was derived in [31] with the assumption that the correlation coefficient is real-valued, although this is not verified by real data.

In this work, a realistic correlated Tomo-SAR model is proposed and the elevation estimation accuracy for the proposed model is derived. Firstly, a correlated residual phase term is introduced in the original Tomo-SAR model, and then the total noise signal is formulated by two parts: one is the correlated residual phase term due to dominant targets and the other one is the additive noise originated from the thermal effect of the system and correlated clutters. Subsequently, the joint correlated Tomo-SAR model is formed by theoretical analysis. Then, with the joint probability density function (pdf) of observations and the random disturbance parameters, the elevation accuracy of scatters is derived under the framework

Huaping Xu is the corresponding author. Manuscript received X X, X; revised X X, X. This work was funded by the National Natural Science Foundation of China under Grant No. 61471020.

B. Yang, H. Xu, Y. You are with the School of Electronic and Information Engineering, Beihang University, Beijing 100191, China (e-mail: yangb89@buaa.edu.cn, xuhuaping@buaa.edu.cn and yyngc@126.com).

W. Liu is with the Department of Electronic and Electrical Engineering, University of Sheffield, Sheffield S1 3JD, U.K.(e-mail: w.liu@sheffield.ac.uk).

X. Xie is with the College of Science, Northwest A&F University, Yangling, Shaanxi 712100, China (e-mail: xiexzh@nwafu.edu.cn).

[1]Some works denote the Cramér-Rao bound by CRLB and the hybrid Cramér-Rao bound by PCRB (Posterior Cramér-Rao bound) or MCRLB (Modified Cramér-Rao lower bound).

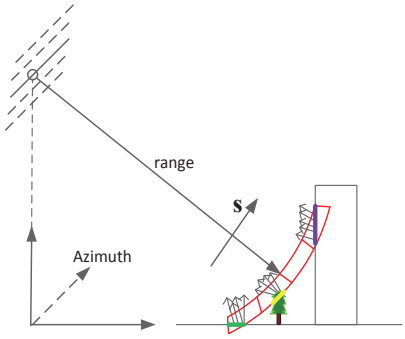

Fig. 1. Radar side-looking imaging geometry, where each azimuth-range pixel value is the superposition of echoes reflected from all targets in the referred red sector area.

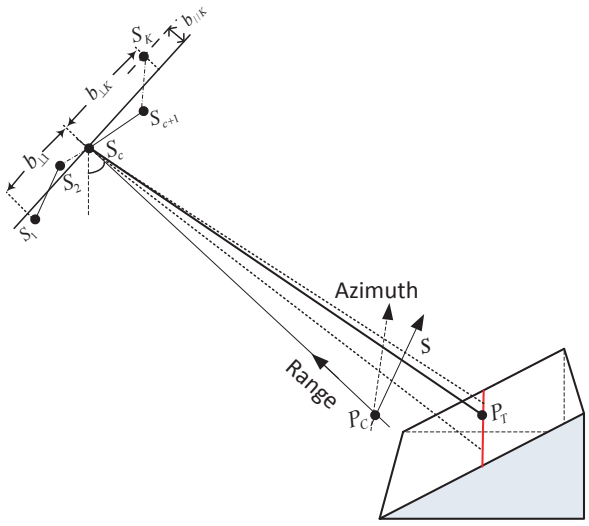

Fig. 2. Baseline distribution of the Tomo-SAR system and one man-made scene, where pixels corresponding to the red resolution cell have the same elevation support.

of HCRB. Furthermore, a simplified calculation of the HCRB is proposed when the bound for elevation estimation is the main focus. Finally, some factors affecting the proposed bound are studied for the case with one and two scatterers. Detailed analysis and simulation results as well as real data validation show that the HCRB under the residual correlated phase and correlated additive noise is more realistic than the CRB derived with perfect phase calibration and additive white noise assumption, and the CRB presented in [8] and [16] can be considered as a special case of our result.

The rest of this paper is organized as follows. In Section II, a review of the Tomo-SAR model is provided, followed by the proposed correlated Tomo-SAR model in Section III. The HCRB for elevation estimation with correlated noise is presented in Section IV, and the derived bound is analysed for the case with single and two scatterers and verified by two CS-based estimators in Section V, followed by real data validation. Finally, conclusions are drawn in Section VI.

II. Original Tomo-SAR model

In the side-looking imaging geometry shown in Fig. 1, each azimuth-range pixel value is the superposition of echoes reflected from targets in the referred red sector area. That is, each pixel in a single look complex (SLC) image represents the projection of a 3-D sector area onto the azimuth-range plane along the elevation direction. The k-th high-resolution SAR image followed by co-registration and phase compensation (deramping, atmospheric and deformation phase removal [32], [33]) can be modeled by the following line integration [3], [4]

$$y_k \approx \int_{[S_{min},\, S_{max}]} x(s)\exp(j2\pi\xi_k s)ds \tag{1}$$

where $[S_{min},\, S_{max}]$ is the elevation range along the direction s, $j=\sqrt{-1}$, ξ_k denotes the elevation frequency with $\xi_k = -2b_{\perp k}/\lambda r$, λ and r are radar wavelength and the range of the considered cell, respectively, and $b_{\perp k}$ is the effective baseline perpendicular to the range direction of the master antenna as shown in Fig. 2.

Similar to uniform partition of the red sector area in Fig. 1, the integration on elevation s is usually discretized with N uniform segments in $[S_{min},\, S_{max}]$. The pixel value of the k-th observation y_k can be written as a linear combination of M strong and sparse backscattering sources

$$y_k = \sum_{m=1}^{M} \mathbf{\Phi}(k,m)x_m + w_k \tag{2}$$

where $\mathbf{\Phi}(k,m) = \exp(-j2\pi\xi_k s_m)$ for $k = 1, 2, \cdots, K$ and $m = 1, 2, \cdots, M$, s_m and x_m are the elevation and complex reflectivity of the m-th target, respectively, and w_k is the additive noise containing clutters and thermal noise.

Furthermore, the K sets of tomographic SAR data can be modeled linearly as one stack [3]–[5]

$$\mathbf{y} = \mathbf{\Phi x} + \mathbf{w} \tag{3}$$

where $\mathbf{y}$ is the observations with $K \times 1$ elements in referred azimuth-range cell, $\mathbf{\Phi}$ is a semi-discrete space-frequency matrix along direction $\mathbf{s}$ with $K \times N$ elements, and $\mathbf{x} = [x_1, \cdots, x_N]^{\mathrm{T}}$ is the complex reflectivity vector with M nonzero elements. For example, there are many uniform partitions of the red sector area in $[S_{min},\, S_{max}]$, but only the scattering of ground and tree canopy as well as building facades is effective. Considering the case that vertical baselines $\{b_{\perp k}\}_{k=1}^{K}$ are distributed uniformly with equal spacing, i.e., the interval of the two adjacent satellites ΔB is equal, the n-th column of $\mathbf{\Phi}$ in the model of tomographic SAR can be expressed as

$$\mathbf{\Phi}(s_n) = [\mathrm{e}^{-j4\pi\frac{\lfloor \frac{K}{2} \rfloor \Delta B s_n}{\lambda r}}, \cdots, 1, \cdots, \mathrm{e}^{j4\pi\frac{\lceil \frac{K}{2}-1 \rceil \Delta B s_n}{\lambda r}}]^{\mathrm{T}} \tag{4}$$

where $\lfloor\cdot\rfloor$ denotes the round down to integer operation, while $\lceil\cdot\rceil$ denotes the round up to integer operation. The cluttering effect is normally embedded in the additive white noise contribution. Thus, $\mathbf{w}$ is assumed to be zero-mean Gaussian with a covariance matrix $\sigma_{\mathrm{w}}^2\mathbf{R}_{\mathrm{w}}$, where σ_{w}^2 is the intensity of noise and $\mathbf{R}_{\mathrm{w}}$ is the $K \times K$ identity matrix [3]–[13].

For the real spaceborne SAR data, on the one hand, the baseline parameters and ranges of the neighboring pixels in Eq. (3) are approximately equal, and therefore the observed

matrices of the neighboring stacks can be expressed in the same form; on the other hand, the targets' elevation of range line cells, e.g. the cells represented by the red line area in the triangular slope facet of Fig. 2, is almost equal to each other. Thus, some neighboring stacks are modeled with approximately the same space-frequency matrix and elevation support.

After L pixel stacks or multiple channels are selected, the Tomo-SAR data is combined into the following joint model [16], [17], [34], [35]

$$\begin{cases} \mathbf{y}_1 = \mathbf{\Phi}\mathbf{x}_1 + \mathbf{w}_1 \\ \mathbf{y}_2 = \mathbf{\Phi}\mathbf{x}_2 + \mathbf{w}_2 \\ \quad\quad\vdots \\ \mathbf{y}_L = \mathbf{\Phi}\mathbf{x}_L + \mathbf{w}_L \end{cases} \tag{5}$$

or alternatively into the following form

$$\mathbf{Y} = \mathbf{\Psi}\mathbf{X} + \mathbf{W} \tag{6}$$

where $\mathbf{X} = [\mathbf{x}_1^{\mathrm{T}} \cdots \mathbf{x}_L^{\mathrm{T}}]^{\mathrm{T}}$, $\mathbf{Y} = [\mathbf{y}_1^{\mathrm{T}} \cdots \mathbf{y}_L^{\mathrm{T}}]^{\mathrm{T}}$, $\mathbf{W} = [\mathbf{w}_1^{\mathrm{T}} \cdots \mathbf{w}_L^{\mathrm{T}}]^{\mathrm{T}}$, and $\mathbf{\Psi}$ is a block diagonal matrix with $\mathbf{\Phi}$ being the main diagonal elements. When $L = 1$, the joint model is reduced to the single model in Eq. (3).

III. JOINT CORRELATED TOMO-SAR MODEL

In the preprocessing of Tomo-SAR, the phase part not related to elevation estimation should be compensated first, such as the deramping phase and atmospheric phase as well as the deformation phase. The residual phase term after compensation is expressed as $\exp(-j\theta_k)$ and then incorporated into Eq. (2). The k-th observation can be expressed by

$$y_k = \sum_{m=1}^{M} \exp(-j\theta_k)\mathbf{\Phi}(k,m)x_m + \hat{w}_k \tag{7}$$

where θ_k is the residual noise phase related to uncompensated phase and multiplicative speckle noise, and $\hat{w}_k$ denotes the noise generated through the thermal effect and the clutters with the residual phase disturbance. As a result, the general Tomo-SAR model in a vector form is given by

$$\mathbf{y} = \sum_{m=1}^{M} \mathbf{a} \odot \mathbf{\Phi}(s_m)x_m + \hat{\mathbf{w}} \tag{8}$$

where $\mathbf{a} = [\exp(-j\theta_1) \cdots \exp(-j\theta_K)]^{\mathrm{T}}$ is the vector form of the residual phase term, $\odot$ is the Hadamard product and $\hat{\mathbf{w}}$ is the vector of additive noise.

The coherence between the elements of the speckle noise phase vector is very strong, enabling it to focus 3-D backscattering profiles [39]. The speckle noise phase can be decomposed into one common phase part and one different phase part. The common part can be attributed to the scattering phase of the dominant scatterer, and then the different phase vector among different observations is weakly correlated. Accordingly, elements of the residual phase vector $\boldsymbol{\theta}$ must be weakly correlated. In this paper, the vector of residual phase is assumed to be multivariate Gaussian and identically distributed with zero mean and covariance matrix $\sigma_\theta^2\mathbf{C}_\theta$, where

$$\mathbf{C}_\theta = \begin{pmatrix} 1 & \rho_{12} & \cdots & \rho_{1K} \\ \rho_{12} & 1 & \cdots & \rho_{2K} \\ \vdots & \vdots & \ddots & \vdots \\ \rho_{1K} & \rho_{2K} & \cdots & 1 \end{pmatrix} \tag{9}$$

with ρ_{mn} representing the correlation coefficient between θ_m and θ_n, and σ_θ^2 is the intensity of residual phase, which is weak after the preprocessing.

Since the linear term in Eq. (2) is the major concern in Tomo-SAR, the model in Eq. (8) can be decomposed into the sum of the ideal target measurement and the total noise term $\mathbf{z}$,

$$\mathbf{y} = \sum_{m=1}^{M} \mathbf{\Phi}(s_m)x_m + \mathbf{z} \tag{10}$$

where

$$\mathbf{z} = \sum_{m=1}^{M} (\mathbf{a} - \mathbf{e}) \odot \mathbf{\Phi}(s_m)x_m + \hat{\mathbf{w}} \tag{11}$$

and $\mathbf{e}$ is an all-one $K \times 1$ vector. Then, the mean vector and covariance matrix of $\mathbf{z}$ are given by

$$\boldsymbol{\mu}_{\mathbf{z}} = (\mu_{\mathrm{a}} - 1) \sum_{m=1}^{M} \mathbf{\Phi}(s_m)x_m \tag{12}$$

$$\mathbf{C}_{\mathbf{z}} = (\sum_{m=1}^{M} \mathbf{H}_m x_m)\mathbf{R}_{\mathrm{c}}(\sum_{m=1}^{M} \mathbf{H}_m x_m)^{\mathrm{H}} + \sigma_{\mathrm{w}}^2\mathbf{R}_{\hat{\mathrm{w}}} \tag{13}$$

where

$$\begin{aligned} \mathbf{R}_{\mathrm{c}} &= \mathbf{R}_{\mathrm{a}} - \mu_{\mathrm{a}}^2\mathbf{e} \cdot \mathbf{e}^{\mathrm{T}} \\ \mu_{\mathrm{a}} &= \exp(-\tfrac{\sigma_\theta^2}{2}) \\ \mathbf{R}_{\mathrm{a}} &= \mu_{\mathrm{a}}^2 \exp(\mathbf{C}_\theta\sigma_\theta^2) \end{aligned} \tag{14}$$

and $\mathbf{H}_m$ denotes the diagonal matrix obtained by diagonalizing the vector $\mathbf{\Phi}(s_m)$. The statistical characteristics of disturbance μ_{a} and $\mathbf{R}_{\mathrm{a}}$ can be obtained based on the property that the Fourier transform of a Gaussian function is another Gaussian function. From Eq. (8), when $\sigma_\theta^2 = 0$ and $\boldsymbol{\theta}$ is equal to zero, we have $\mathbf{z} = \mathbf{w}$ in Eq. (3). As a result, our proposed model can be considered as an extension of the original Tomo-SAR model. Additionally, the weak correlation of the elements in the residual phase vector would result in weak correlation of the elements in the noise vector $\mathbf{z}$. According to the SAR signal model in [40], the k-th element of cluttering signal in Eq. (8) can be expressed as

$$\hat{w}_k = \rho \cdot e^{j2\pi\xi_k\hat{s}} \cdot \omega_k e^{j\varphi_k} \tag{15}$$

where ρ is the common amplitude of the complex reflectivity function, $e^{j2\pi\xi_k\hat{s}}$ is the phase factor related to the background height profile $\hat{s}$ and the k-th antenna position, ω_k is the amplitude of the multiplicative speckle noise, and φ_k is the k-th interferometric phase of the speckle. In [40], interferometric phases of speckle for different observations are weakly correlated for a dual-baseline SAR system, i.e., when the coherences between three images are 0.57, 0.33 and 0.55, the correlation coefficient of interferometric phases is 0.0281. This is the reason why the height profile of background

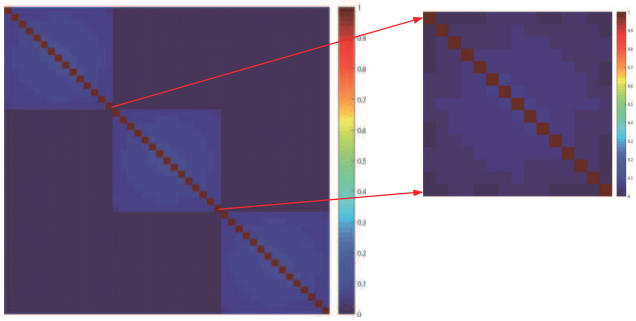

Fig. 3. The amplitude map of the noise covariance matrix $\mathbf{C_Z}$ with $K = 15$ for the case of three stacks.

areas can be estimated in [41]–[43] under the assumption of mutual independence of different interferograms. Therefore, the weak correlation of interferometric phases for a dual-baseline SAR system can be generalized to the Tomo-SAR system. Accordingly, the phases of $\hat{\mathbf{w}}$ are weakly correlated, leading to weak correlation among the elements of $\mathbf{z}$ in Eq. (13).

Based on the above analysis, the additive noise $\hat{\mathbf{w}}$ can be assumed to be multivariate complex Gaussian with zero mean and covariance matrix $\sigma_{\mathrm{w}}^2\mathbf{R}_{\hat{\mathrm{w}}}$. For all stacks, $\mathbf{R}_{\hat{\mathrm{w}}}$ is given by

$$\mathbf{R}_{\hat{\mathrm{w}}} = \begin{pmatrix} 1 & c_{12}^* & \cdots & c_{1K}^* \\ c_{12} & 1 & \cdots & c_{2K}^* \\ \vdots & \vdots & \ddots & \vdots \\ c_{1K} & c_{2K} & \cdots & 1 \end{pmatrix} \tag{16}$$

where c_{mn} is the complex correlation coefficient between $\hat{w}_m$ and $\hat{w}_n$.

After combining the joint Tomo-SAR model in Eq. (5) with the single stack correlated model in Eq. (8), the joint Tomo-SAR correlated model with L stacks can be formulated as

$$\begin{cases} \mathbf{y}_1 = \sum\limits_{m=1}^{M} \mathbf{a}_1 \odot \mathbf{\Phi}(s_m) x_{1m} + \hat{\mathbf{w}}_1 \\ \mathbf{y}_2 = \sum\limits_{m=1}^{M} \mathbf{a}_2 \odot \mathbf{\Phi}(s_m) x_{2m} + \hat{\mathbf{w}}_2 \\ \qquad\qquad \vdots \\ \mathbf{y}_L = \sum\limits_{m=1}^{M} \mathbf{a}_L \odot \mathbf{\Phi}(s_m) x_{Lm} + \hat{\mathbf{w}}_L \end{cases} \tag{17}$$

where $\mathbf{a}_l$ $(l = 1 \cdots L)$ is the multiplicative noise vector for the l-th image, and s_m is the common elevation of targets in L stacks.

Eq. (17) can be combined into the following form

$$\mathbf{Y} = \mathbf{\Psi}\mathbf{X} + \mathbf{Z} \tag{18}$$

where $\mathbf{Z} = [\mathbf{z}_1^{\mathrm{T}} \cdots \mathbf{z}_L^{\mathrm{T}}]^{\mathrm{T}}$ with $\mathbf{z}_l$ $(l = 1 \cdots L)$ formulated in the same way as Eq. (11). When $L = 1$, it is reduced to the single stack model in Eq. (10).

Due to the stationarity of correlated residual phase and correlated additive noise for all pixels, the disturbance vectors in each stack can be assumed to have the same statistics. It is normally assumed that neighboring stacks of one Tomo-SAR image are uncorrelated (Part II of [44]). Without loss of generality, the covariance matrix of the overall noise signal of the joint model $\mathbf{C_Z}$ is block diagonal with $\mathbf{C_z}$ being the main diagonal elements. As an extended example of Eq. (13), $\mathbf{C_Z}$ for the case of three stacks is shown in Fig. 3.

IV. Derivation of the Hybrid Cramér-Rao Bounds

As mentioned, existing works on CRB derivation are based on the assumption that the additive noise is white and the phase is compensated perfectly. Next, we will derive the lower bound for the proposed model (Eq. (17)) under correlated noise.

When the unknown parameters contain both random and deterministic variables, the HCRB is always employed. The deterministic and random parameters are unified in the Fisher information matrix, where the diagonal elements of the covariance matrix represent the bounds of unbiased estimates of deterministic parameters and the mean square errors on the estimates of the random variables. For our case, the unknown parameter vector $\boldsymbol{\xi}$ includes the deterministic parameters in $\boldsymbol{\xi}_d$ and the random parameters in $\boldsymbol{\xi}_r$. Let $\hat{\boldsymbol{\xi}}_d$ be an unbiased estimator of $\boldsymbol{\xi}_d$ and $\hat{\boldsymbol{\xi}}_r$ be an estimator of $\boldsymbol{\xi}_r$. For every estimator, the HCRB ensures that

$$\mathbf{E}_{\mathbf{Y},\boldsymbol{\xi}_r} \begin{bmatrix} (\boldsymbol{\xi}_d - \hat{\boldsymbol{\xi}}_d)(\boldsymbol{\xi}_d - \hat{\boldsymbol{\xi}}_d)^{\mathrm{T}} & (\boldsymbol{\xi}_d - \hat{\boldsymbol{\xi}}_d)(\boldsymbol{\xi}_r - \hat{\boldsymbol{\xi}}_r)^{\mathrm{T}} \\ (\boldsymbol{\xi}_r - \hat{\boldsymbol{\xi}}_r)(\boldsymbol{\xi}_d - \hat{\boldsymbol{\xi}}_d)^{\mathrm{T}} & (\boldsymbol{\xi}_r - \hat{\boldsymbol{\xi}}_r)(\boldsymbol{\xi}_r - \hat{\boldsymbol{\xi}}_r)^{\mathrm{T}} \end{bmatrix} \succeq \mathbf{F}_{\mathbf{h}}^{-1} \tag{19}$$

where $(\cdot)^{\mathrm{T}}$ is the transpose operator and $\mathbf{E}_{\mathbf{Y},\boldsymbol{\xi}_r}[\cdot]$ denotes the expectation with the joint pdf of observations $\mathbf{Y}$ and random parameters $\boldsymbol{\xi}_r$. The symbol $\succeq$ represents that the difference matrix of the left covariance matrix minus the right hybrid information matrix $\mathbf{F_h}$ is nonnegative definite. Since $\mathbf{E}_{\mathbf{Y},\boldsymbol{\xi}_r} = \mathbf{E}_{\boldsymbol{\xi}_r}\left(\mathbf{E}_{\mathbf{Y}|\boldsymbol{\xi}_r}\right)$, $\mathbf{F_h}$ can be expressed as the expectation of the sum of the standard Fisher information matrix $\mathbf{F_c}$ and prior information matrix $\mathbf{F_p}$ with respect to $\boldsymbol{\xi}_r$, that is,

$$\mathbf{F_h}(\boldsymbol{\xi}) = \mathbf{E}_{\boldsymbol{\xi}_r}\left[\mathbf{F_c}(\boldsymbol{\xi})\right] + \mathbf{F_p}(\boldsymbol{\xi}), \tag{20}$$

with

$$\mathbf{F_c}(\boldsymbol{\xi}) = -\mathbf{E}_{\mathbf{Y}|\boldsymbol{\xi}_r}\left[\begin{pmatrix} \frac{\partial^2 \ln p(\mathbf{Y}|\boldsymbol{\xi})}{\partial \boldsymbol{\xi}_d \partial \boldsymbol{\xi}_d^{\mathrm{T}}} & \frac{\partial^2 \ln p(\mathbf{Y}|\boldsymbol{\xi})}{\partial \boldsymbol{\xi}_d \partial \boldsymbol{\xi}_r^{\mathrm{T}}} \\ \frac{\partial^2 \ln p(\mathbf{Y}|\boldsymbol{\xi})}{\partial \boldsymbol{\xi}_r \partial \boldsymbol{\xi}_d^{\mathrm{T}}} & \frac{\partial^2 \ln p(\mathbf{Y}|\boldsymbol{\xi})}{\partial \boldsymbol{\xi}_r \partial \boldsymbol{\xi}_r^{\mathrm{T}}} \end{pmatrix}\right] \tag{21}$$

$$\mathbf{F_p}(\boldsymbol{\xi}) = -\mathbf{E}_{\boldsymbol{\xi}_r}\left[\begin{pmatrix} \mathbf{0} & \mathbf{0} \\ \mathbf{0} & \frac{\partial^2 \ln p(\boldsymbol{\xi}_r)}{\partial \boldsymbol{\xi}_r \partial \boldsymbol{\xi}_r^{\mathrm{T}}} \end{pmatrix}\right] \tag{22}$$

where $\mathbf{E}_{\mathbf{Y}|\boldsymbol{\xi}_r}[\cdot]$ denotes the conditional expectation with respect to $p(\mathbf{Y}|\boldsymbol{\xi})$.

Following the analysis of the joint correlated model in Section III and the HCRB theory above, the HCRB on elevation is derived according to the Gaussian pdf of residual phase. For the two types of unknown parameters in $\boldsymbol{\xi}$, $\boldsymbol{\xi}_d$ includes the noise intensity σ_{w}^2, the weak correlation matrix $\mathbf{R}_{\hat{\mathrm{w}}}$, all M elevation positions s_m $(m = 1, 2, \cdots, M)$, the amplitude $|x_{ml}|$ and phase ϕ_{ml} of the m-th source in the l-th stack for $m = 1, 2, \cdots, M$ and $l = 1, 2, \cdots, L$, while $\boldsymbol{\xi}_r$ includes the residual phase θ_{kl} for $k = 1, 2, \cdots, K$ and $l = 1, 2, \cdots, L$. In detail,

$$\boldsymbol{\xi}_d = [\sigma_{\mathrm{w}}^2, \mathbf{R}_{\hat{\mathrm{w}}}, |x_{11}|, \phi_{11}, s_1, \cdots, |x_{ML}|, \phi_{ML}, s_M]^{\mathrm{T}} \tag{23}$$

$$\boldsymbol{\xi}_r = [\theta_{11}, \cdots, \theta_{KL}]^{\mathrm{T}} \tag{24}$$

Note that the dimension of $\boldsymbol{\xi}_d$ and $\boldsymbol{\xi}_r$ is $(M+2ML+\frac{K(K-1)}{2}+1)\times 1$ and $KL\times 1$, respectively.

Under the condition of the unknown parameter $\boldsymbol{\xi}$, the observed data $\mathbf{Y}$ follows the complex Gaussian distribution with a mean value $\boldsymbol{\mu}(\boldsymbol{\xi})$ and covariance matrix $\mathbf{C}(\boldsymbol{\xi})$ as

$$\boldsymbol{\mu}(\boldsymbol{\xi}) = [(\mathbf{A}_1\boldsymbol{\Phi}\mathbf{x}_1)^{\mathrm{T}}\cdots(\mathbf{A}_L\boldsymbol{\Phi}\mathbf{x}_L)^{\mathrm{T}}]^{\mathrm{T}} \tag{25}$$

$$\mathbf{C}(\boldsymbol{\xi}) = \sigma_{\mathrm{w}}^2\mathbf{I}_L\otimes\mathbf{R}_{\hat{\mathrm{w}}} \tag{26}$$

where $\mathbf{A}_l$ is the diagonal matrix of $\mathbf{a}_l$ for $l=1,2,\cdots,L$ and $\mathbf{I}_L$ is an $L\times L$ identity matrix. Accordingly, the likelihood function of $\mathbf{Y}$ is given by

$$p(\mathbf{Y}|\boldsymbol{\xi}) = \frac{\exp[-(\mathbf{Y}-\boldsymbol{\mu}(\boldsymbol{\xi}))^{\mathrm{H}}\mathbf{C}(\boldsymbol{\xi})^{-1}(\mathbf{Y}-\boldsymbol{\mu}(\boldsymbol{\xi}))]}{\pi^{KL}|\mathbf{C}(\boldsymbol{\xi})|} \tag{27}$$

where $(\cdot)^{\mathrm{H}}$ is the Hermitian transpose. By referring to [45], the first-order derivative of the log-likelihood function is given by

$$\begin{aligned}\frac{\partial}{\partial\boldsymbol{\xi}}\ln p(\mathbf{Y}|\boldsymbol{\xi}) = &-tr\left[\mathbf{C}(\boldsymbol{\xi})^{-1}\frac{\partial\mathbf{C}(\boldsymbol{\xi})}{\partial\boldsymbol{\xi}}\right]\\ &+\mathbf{Y}^{\mathrm{H}}\mathbf{C}(\boldsymbol{\xi})^{-1}\frac{\partial\mathbf{C}(\boldsymbol{\xi})}{\partial\boldsymbol{\xi}}\mathbf{C}(\boldsymbol{\xi})^{-1}\mathbf{Y}\end{aligned} \tag{28}$$

where $tr(\cdot)$ denotes the trace of the matrix. Then, the (p,q) element of the standard Fisher information matrix is

$$\begin{aligned}[\mathbf{F}_{\mathbf{c}}(\boldsymbol{\xi})]_{pq} = &\,2\,Re\left(\frac{\partial\boldsymbol{\mu}(\boldsymbol{\xi})^{\mathrm{H}}}{\partial\xi_p}\mathbf{C}(\boldsymbol{\xi})^{-1}\frac{\partial\boldsymbol{\mu}(\boldsymbol{\xi})}{\partial\xi_q}\right)\\ &+tr\left[\mathbf{C}(\boldsymbol{\xi})^{-1}\frac{\partial\mathbf{C}(\boldsymbol{\xi})}{\partial\xi_p}\mathbf{C}(\boldsymbol{\xi})^{-1}\frac{\partial\mathbf{C}(\boldsymbol{\xi})}{\partial\xi_q}\right]\end{aligned} \tag{29}$$

for $p,q=1,2,\cdots,M+2ML+1$, where $Re(\cdot)$ denotes the real part of a complex matrix. Without considering the random parameters $\boldsymbol{\xi}_r$, the standard Fisher information matrix (Eq. (21)) was used to derive the CRB in [16].

Since the random nuisance parameter only contains the residual phase, which is multivariate Gaussian, the derivative of log-prior function with respect to this nuisance parameter can be obtained by

$$\frac{\partial}{\partial\boldsymbol{\xi}_r}\ln p(\boldsymbol{\xi}_r) = \frac{\partial}{\partial\boldsymbol{\xi}_r}(-\frac{\sum_{l=1}^{L}\boldsymbol{\theta}_l^{\mathrm{T}}\mathbf{C}_\theta^{-1}\boldsymbol{\theta}_l}{2\sigma_\theta^2}) \tag{30}$$

Substituting (21), (22), (28) and (30) into (20), the hybrid Fisher information matrix $\mathbf{F_h}$ can be written as

$$\begin{aligned}[\mathbf{F_h}(\boldsymbol{\xi})]_{pq} = &\,\mathbf{E}_{\boldsymbol{\xi}_r}\left\{2Re\left[\frac{\partial\boldsymbol{\mu}(\boldsymbol{\xi})^{\mathrm{H}}}{\partial\xi_p}\mathbf{C}(\boldsymbol{\xi})^{-1}\frac{\partial\boldsymbol{\mu}(\boldsymbol{\xi})}{\partial\xi_q}\right]\right\}\\ &+tr\left[\mathbf{C}(\boldsymbol{\xi})^{-1}\frac{\partial\mathbf{C}(\boldsymbol{\xi})}{\partial\xi_p}\mathbf{C}(\boldsymbol{\xi})^{-1}\frac{\mathbf{C}(\boldsymbol{\xi})}{\partial\xi_q}\right]\\ &+\mathbf{E}_{\boldsymbol{\xi}_r}\left[\frac{1}{2\sigma_\theta^2}\frac{\partial^2}{\partial\xi_p\xi_q}\left(\sum_{l=1}^{L}\boldsymbol{\theta}_l^{\mathrm{T}}\mathbf{C}_\theta^{-1}\boldsymbol{\theta}_l\right)\right]\end{aligned} \tag{31}$$

for $p,q=1,2,\cdots,M+2ML+\frac{K(K-1)}{2}+1+KL$.

$$\mathbf{F_h}(\xi) = \begin{array}{c} \\ \boldsymbol{\xi}_{d1}\\ \boldsymbol{\xi}_{d2}\\ \boldsymbol{\xi}_{r}\end{array}\begin{array}{c}\begin{array}{ccc}\boldsymbol{\xi}_{d1} & \boldsymbol{\xi}_{d2} & \boldsymbol{\xi}_{r}\end{array}\\ \begin{pmatrix}\mathbf{F}_1 & 0 & 0\\ 0 & \mathbf{F}_2 & \mathbf{F}_{23}\\ 0 & \mathbf{F}_{23}^{\mathrm{H}} & \mathbf{F}_3\end{pmatrix}\end{array}$$

Fig. 4. Structure of the complete hybrid Fisher information matrix.

A. HCRB of Elevation

Applying the derivatives with respect to arbitrary parameters ξ_p and ξ_q in $\boldsymbol{\xi}$ and then the expectation with respect to $\boldsymbol{\xi_r}$ in Appendix A, the complete hybrid Fisher information matrix $\mathbf{F_h}$ can be obtained. Then, the HCRB for elevation in the presence of correlated noise is

$$\sigma^2(s_m) = \left[\mathbf{F_h}^{-1}(\boldsymbol{\xi})\right]_{s_m} \tag{32}$$

where the subscript s_m denotes the diagonal element of the inverse matrix corresponding to the elevation of the m-th source. Since the deterministic parameters $\boldsymbol{\xi}_{d1}=[\sigma_{\mathrm{w}}^2,\mathbf{R}_{\hat{\mathrm{w}}}]^{\mathrm{T}}$ are not correlated with $\boldsymbol{\xi}_{d2}=[|x_{11}|,\phi_{11},s_1,\cdots,|x_{ML}|,\phi_{ML},s_M]^{\mathrm{T}}$ and the random parameters $[\theta_{11},\cdots,\theta_{KL}]$, the complete hybrid Fisher information matrix can be partitioned into the block form shown in Fig. 4. As the bound for elevation estimation is the major concern in Tomo-SAR, we can just select the submatrix highlighted in gray in Fig. 4. Accordingly, the derivation with respect to $\boldsymbol{\xi}_{d1}$ in Eq. (32) can be omitted. Thus, the bound for elevation estimation can be calculated by

$$\sigma^2(s_m) = \begin{pmatrix}\mathbf{F}_2(\boldsymbol{\xi}) & \mathbf{F}_{23}(\boldsymbol{\xi})\\ \mathbf{F}_{23}(\boldsymbol{\xi})^{\mathrm{H}} & \mathbf{F}_3(\boldsymbol{\xi})\end{pmatrix}^{-1}_{s_m} \tag{33}$$

where the partitioned submatrix can be calculated with

$$\begin{aligned}[\mathbf{F_h}(\boldsymbol{\xi})]_{pq} = &\,\mathbf{E}_{\boldsymbol{\xi}_r}\left\{2Re\left[\frac{\partial\boldsymbol{\mu}(\boldsymbol{\xi})^{\mathrm{H}}}{\partial\xi_p}\mathbf{C}(\boldsymbol{\xi})^{-1}\frac{\partial\boldsymbol{\mu}(\boldsymbol{\xi})}{\partial\xi_q}\right]\right\}\\ &+\frac{1}{2\sigma_\theta^2}\mathbf{E}_{\boldsymbol{\xi}_r}\left[\frac{\partial^2}{\partial\xi_p\partial\xi_q}(\sum_{l=1}^{L}\boldsymbol{\theta}_l^{\mathrm{T}}\mathbf{C}_\theta^{-1}\boldsymbol{\theta}_l)\right]\end{aligned} \tag{34}$$

for $p,q=(\frac{K(K-1)}{2}+2),\cdots,M+2ML+\frac{K(K-1)}{2}+1+KL$.

V. Simulations and Results

In this section, simulations are performed to examine the derived HCRB under correlated noise for cases with one scatterer and two scatterers, respectively, which have been the focus of many works on detection and estimation [46]–[51]. The baselines are evenly distributed in all simulations and part of the parameters listed in Table I.

As shown by Eq. (11), the total noise term is composed of the multiplicative noise part and the additive noise part. Accordingly, the total noise effect is divided into two parts: the effect of additive noise is measured by the SNR, which is the ratio of the power of signal and the power of additive noise $\hat{\mathbf{w}}$

$$\mathrm{SNR}_m = 10\lg(|x_m|^2/\sigma_{\mathrm{w}}^2), m=1\cdots M \tag{35}$$

TABLE I
EXPERIMENTAL PARAMETERS

wavelength (λ)	0.03125 m
view angle	20 deg
range distance (r)	553.37 Km
correlation coefficient ρ_{mn} $(1 \leq m \neq n \leq K)$	0.01
lower triangular elements of $\mathbf{R}_{\hat{\mathbf{w}}}$ $(C_{mn}, m > n)$	0.01 + 0.01 j
upper triangular elements of $\mathbf{R}_{\hat{\mathbf{w}}}$ $(C_{mn}, m < n)$	0.01 - 0.01 j

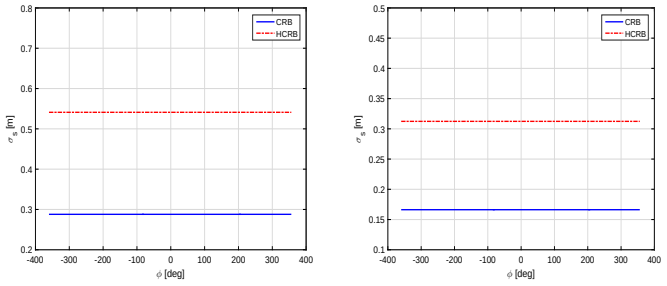

(a) (b)

Fig. 5. The elevation accuracy of CRB and HCRB as a function of the phase ϕ. Parameters: $M = 1$, vertical baseline span $B = 400$m, satellite number $K = 25$, SNR=15dB, σ_θ^2=0.04. (a) Single stack; (b) three stacks.

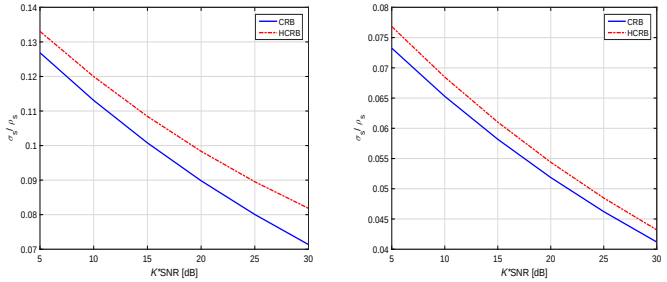

(a) (b)

Fig. 6. The elevation accuracy of CRB and HCRB over Rayleigh resolution as a function of the product of satellite number and SNR.Parameters: $M = 1$, vertical baseline span $B = 300$m, ϕ=0, σ_θ^2=0.04. (a) Single stack; (b) three stacks.

where $|x_m|$ is the amplitude of the m-th dominant target; the effect of multiplicative noise is measured by the variance of residual phase σ_θ^2.

Firstly, HCRB results with respect to some parameters are provided to analyze the influencing factors. We will also show that the bounds of the joint model are better than that of the single model. Then, simulation results are provided to demonstrate that the derived HCRBs for the correlated model are more realistic than those for the original model. Finally, the superiority of the proposed HCRB is further validated through real data experiment.

A. HCRB Analysis

Firstly, when one scatterer is considered, the elevation HCRB as a function of the scattering phase ϕ of this single scatterer, SNR and the number of observations K are shown in Figs. 5 and 6 for both single stack and three stacks. It's observed from Fig. 5 that the elevation accuracy does not change with ϕ, which indicates that ϕ has no influence on the HCRB when there is only one scatterer in the azimuth-range

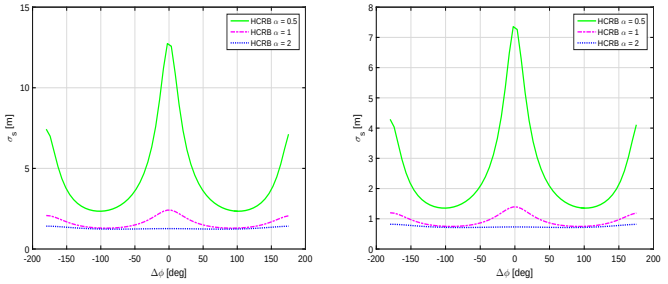

(a) (b)

Fig. 7. The elevation accuracy of HCRB as a function of the phase difference $\Delta\phi$ of two sources with different α. Parameters: $M = 2$, $K = 15$, SNR_1 = SNR_2 = 10dB, vertical baseline span $B = 300$m, σ_θ^2=0.04. (a) Single stack; (b) three stacks.

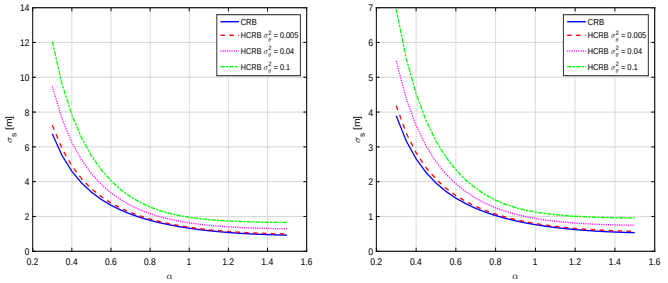

(a) (b)

Fig. 8. The elevation accuracy of CRB and HCRB by integrating $\Delta\phi$ over one period as a function of the super-resolution factor α between two sources with different σ_θ^2. Parameters: $M = 2$, $K = 15$, SNR_1 = SNR_2 = 10dB, vertical baseline span $B = 300$m. (a) Single stack; (b) three stacks.

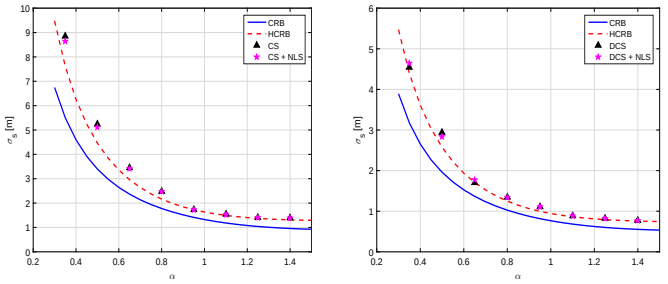

(a) (b)

Fig. 9. CRB and HCRB on the estimation of elevation and variance of two estimators on elevation with respect to α. Parameters: $M = 2$, $K = 15$, SNR_1 = SNR_2 = 10dB, vertical baseline span $B = 300$m, σ_θ^2=0.04. (a) Single stack; (b) three stacks.

pixel. Since the SNR and the number of acquisitions basically play the same role in the estimation, it is observed that the variance of elevation estimation over Rayleigh resolution is approximately linearly proportional to their product for both single and joint cases from Fig. 6.

Now we consider the case with two strong scatterers. A super-resolution factor $\alpha = \frac{\Delta_s}{\rho_s}$ is introduced to measure the distance between them, where Δ_s and ρ_s denote the distance difference of the two scatterers and Rayleigh resolution on elevation, respectively. In terms of the phase difference with different values of α as shown in Fig. 7, when the distance between them increases, the HCRB becomes less dependent on the phase difference. Moreover, the curves have a similar shape for the single and joint cases. When it comes to super-

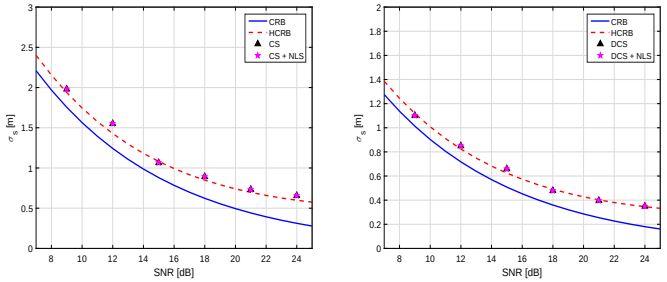

(a) (b)

Fig. 10. CRB and HCRB on the estimation of elevation and variance of two estimators on elevation with respect to SNR. Parameters: $M = 2$, $K = 21$, vertical baseline span $B = 300$m, super-resolution factor $\alpha = 0.8$, σ_θ^2=0.02. (a) Single stack; (b) three stacks.

resolution for two close scatterers, the phase difference has the minimum interference to elevation estimation at $\pm\frac{\pi}{2}$, while 0 and $\pm\pi$ are in the opposite. As shown in Fig. 8, the error increases when they move closer to each other. Furthermore, the larger the variance of the residual phase σ_θ^2, the larger the estimation error. When σ_θ^2 becomes small, the residual phase is very close to zero and the correlation of noise becomes weak, and finally, the elevation result of HCRBs approaches that of CRBs in [8], [16]. As expected, for all above comparisons between the single and multiple stacks, the elevation bound of the joint model is better than that of individual model under the same set of parameters. In addition, from all figures we can see that CRB and HCRB have similar trends.

B. HCRBs versus CRBs

Since the layover separation is the focus of Tomo-SAR, experiments are carried out by groups of simulated observations overlaid by two dominant scatterers. The two targets are distributed in the scene like a step along the azimuth direction. With the parameters listed in Tab I, simulated data for cases of $L = 1$ and $L = 3$ are firstly generated following the model of Eqs. (10) and (18), respectively. Secondly, due to the weak correlation of noise, the basic models of CS Tomo-SAR estimator [11] and DCS Tomo-SAR estimator [17] are directly applied in the correlated model to estimate the elevation for the case of one stack and three stacks. Finally, the estimated variance of Monte-Carlo simulations is computed to compare the HCRB and CRB with the estimation results based on CS and DCS.

The CS Tomo-SAR estimator applied in correlated model for one stack (Eq. (10)) is shown below

$$\hat{\mathbf{x}} = arg\min_{\mathbf{x}} \|\mathbf{x}\|_1 \quad s.t. \ \|\mathbf{y} - \mathbf{\Phi x}\|_2 \leq \varepsilon \tag{36}$$

where ε is the allowed reconstruction error and related to the intensity of noise, $\|\cdot\|_1$ and $\|\cdot\|_2$ denote l_1 and l_2 norms of a vector, respectively.

For the case of joint correlated Tomo-SAR model, three stacks are combined in a measurement matrix $\mathbf{G} = [\mathbf{y}_1, \mathbf{y}_2, \mathbf{y}_3]$, and the reflectivity vectors are placed in a matrix of $\mathbf{\Gamma} = [\mathbf{x}_1, \mathbf{x}_2, \mathbf{x}_3]$. Then, the DCS Tomo-SAR estimator for three stacks correlated model (Eq. (18)) is given by

$$\hat{\mathbf{\Gamma}} = arg\min_{\mathbf{\Gamma}} \|\mathbf{\Gamma}\|_{2,1} \quad s.t. \ \|\mathbf{G} - \mathbf{\Phi\Gamma}\|_F \leq \varepsilon \tag{37}$$

TABLE II
USED TERRASAR-X/TANDEM-X DATA

Mission	date	$b_\perp$
TSX	20120122	77.2771m
TSX	20120213	-171.2727m
TSX	20120306	56.9760m
TSX	20120328	-107.1363m
TSX	20120511	0m
TSX	20120920	-45.6784m
TSX	20121023	-46.3148m
TSX	20130304	-115.1926m
TDX	20130520	222.0882m
TDX	20130622	321.7421m
TDX	20130714	248.0137m
TDX	20130816	-26.4968m
TDX	20130918	22.0632m
TDX	20131010	20.6752m
TDX	20131123	-127.1331m
TDX	20140106	-90.5094m
TDX	20140219	118.2358m
TSX	20140518	-40.0007m
TSX	20140701	10.6413m
TSX	20140814	-22.3069m

where $\|\cdot\|_F$ is the Frobenius norm, and the minimization is for the sum of l_2 norms of all matrix rows. The nonlinear least squares (NLS) strategy is used for refining the estimated results of Eqs. (36) and (37). Finally, the elevations of scatterers are determined by peak positions of the elevation spectrum.

Due to randomness of the phase difference, the elevation bounds are usually calculated by integrating $\Delta\phi$ over one period [8]. Figs. 9 and 10 show both theoretical and simulated results for cases of $L = 1$ and $L = 3$ as a function of α and SNR, respectively, where the variance is adopted to evaluate the estimators in comparison with the derived bounds. It is observed that the elevation estimation result of CS and DCS estimators approaches the HCRBs under correlated noise better than CRBs derived under i.i.d. noise in both simulations and clearly the proposed HCRB provides a tighter bound than the latter one, which also demonstrates the effectiveness of the adopted correlated noise model.

C. Validation through real data

Now we validate the performance of the HCRB by real data, acquired by the sensors of TerraSAR-X/Tandem-X, over Terminal 3-E (T3-E) of the Beijing Capital International Airport, between 2012 and 2014. The maximum height of T3-E is about 45m and the roof of the building has a streamlined shape [52]. 20 passes are used whose observing dates and effective baselines are summarized in Table II. The theoretical resolution is 19.3402m in elevation, which corresponds to 11.0053m in height. Mean effective baseline separation is 25.9481m, and thus the Nyquist elevation span is 367.4641m, which corresponds to 209.1008m of total height span. Fig. 11 (a) shows the intensity of the investigated building, with the corresponding optical image shown in Fig. 11 (b). We study the areas marked in red boxes of Fig. 11 (a) to validate the proposed bound. These azimuth-range cells are overlayed by the eaves of the building and the ground. Additionally, the eaves in the marked areas have a similar height relative to the

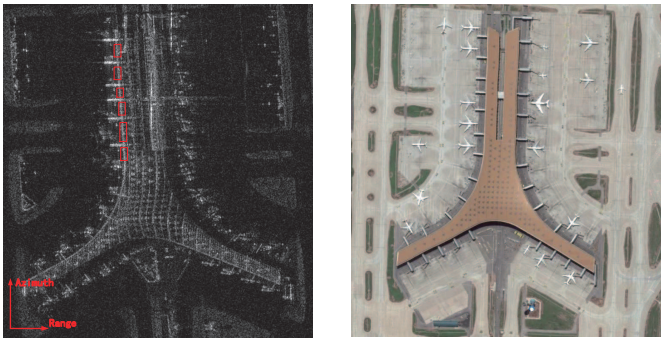

(a) (b)

Fig. 11. T3-E of Beijing Capital International Airport. (a) TerraSAR-X intensity image; (b) Optical image (Google Earth).

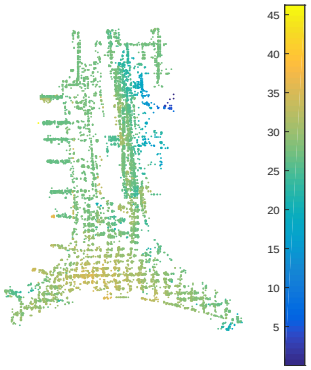

Fig. 12. The reconstructed height profile of the T3-E building using the CS+NLS estimator. It is worth noting that when two scatters are overlaid in one pixel only the point cloud of the stronger scatterer is shown.

ground, and the ground scatters overlayed in the eave pixels are rarely interfered by airplanes.

After data have been registered, calibrated in terms of phase and amplitude by referring to [3]–[5], the elevation point cloud of the T3-E building is reconstructed by the CS+NLS estimator. Then, the height profile is obtained by elevation times the sine of incidence angle. The height profile of the T3-E building is shown in Fig. 12, where we can see clearly the streamline of the roof and the height range is also consistent with the information of T3-E given in [52]. It is worth noting that there exists some bias for the airport covered bridges resulting from the changes due to the presence and absence of airplanes. Subsequently, we choose the stacks with close reflectivity by Kolmogorov-Smirnov test in [34], where two scatterers are detected. In total 23 stacks are selected. The elevation differences of two scatterers of the 23 selected stacks obtained by CS and CS + NLS estimators are shown in Fig. 13 (a), and it is observed that the elevation differences are distributed between 44m and 55m. The standard deviations of the 23 elevation differences based on the CS and CS + NLS are 3.0013m and 2.8707m, respectively. On the assumption of equivalent elevation standard deviations of the two scatterers, the errors of the two estimators are 2.1223m and 2.0299m, respectively.

As mentioned previously, when the number of observations is fixed, the main factors affecting the theoretical bounds, the CRB and HCRB, are α, SNR and σ_θ^2. The elevation

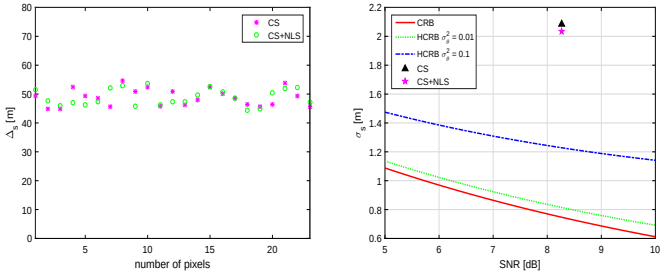

(a) (b)

Fig. 13. Results for the marked region in Fig. 11 (a). (a) The estimated elevation differences of two scatters; (b) theoretical bounds compared with standard deviations of two estimators (parameters: $M = 2$, $K = 20$, vertical baselines are given in Tab. II, super-resolution factor $\alpha = 2.5$).

interval of two close scatterers is about 48.8034m, obtained by averaging the results of CS + NLS, and then we have $\alpha = 2.5$. Furthermore, we can obtain the SNR 8.27dB of each scatter by averaging the 19 cross-channel SNRs, each of which is estimated based on the maximum likelihood method in [53]. Then, we draw the theoretical bounds with respect to the SNR in range from 5dB to 10dB. It is observed from Fig. 13 (b) that the estimated standard deviations from the CS and CS + NLS are greater than the CRB and HCRB. Additionally, the proposed HCRB is closer than CRB to the standard deviations calculated with the real data, especially when σ_θ^2 grows.

VI. Conclusion

In this work, a joint correlated Tomo-SAR model has been provided by introducing the residual phase and correlation coefficient of additive noise. The elevation estimation accuracy for the correlated model was derived in detail using a general HCRB. Some factors affecting the elevation estimation accuracy were studied for one and two scatters to compare HCRB and CRB, respectively. As expected, the joint model has provided a better estimation than that of the single stack model. It was shown from both simulations and real data that the derived HCRB under the residual correlated phase and additive correlated noise is more realistic than the CRB derived based on i.i.d. noise for real scenes. The variance of residual phase is the major factor influencing the difference between HCRB and CRB.

Appendix A

The procedure for calculating the hybrid Fisher information matrix in Eq. (31) is divided into three steps: calculating the derivatives with respect to deterministic and random parameters, followed by taking the expectation with respect to $\boldsymbol{\xi_r}$.

A. Deterministic Parameters

The derivatives of mean $\boldsymbol{\mu}(\boldsymbol{\xi})$ and covariance $\mathbf{C}(\boldsymbol{\xi})$ with respect to parameters from $\boldsymbol{\xi}_d$ can be derived as

$$\begin{aligned}
\frac{\partial \boldsymbol{\mu}(\boldsymbol{\xi})}{\partial \sigma_{\mathrm{w}}^2} &= \mathbf{0}_{KL\times 1} \\
\frac{\partial \boldsymbol{\mu}(\boldsymbol{\xi})}{\partial c_{mn}} &= \mathbf{0}_{KL\times 1} \\
\frac{\partial \boldsymbol{\mu}(\boldsymbol{\xi})}{\partial |x_{ml}|} &= [\mathbf{0}_{K\times 1}^{\mathrm{T}} \cdots (\mathbf{A}_l \boldsymbol{\Phi}(s_m) e^{j\phi_{ml}})^{\mathrm{T}} \cdots \mathbf{0}_{K\times 1}^{\mathrm{T}}]^{\mathrm{T}} \\
\frac{\partial \boldsymbol{\mu}(\boldsymbol{\xi})}{\partial \phi_{ml}} &= [\mathbf{0}_{K\times 1}^{\mathrm{T}} \cdots (j\mathbf{A}_l \boldsymbol{\Phi}(s_m) x_{ml})^{\mathrm{T}} \cdots \mathbf{0}_{K\times 1}^{\mathrm{T}}]^{\mathrm{T}} \\
\frac{\partial \boldsymbol{\mu}(\boldsymbol{\xi})}{\partial s_m} &= [(\mathbf{A}_1 \frac{\partial \boldsymbol{\Phi}(s_m)}{\partial s_m} x_{m1})^{\mathrm{T}} \cdots (\mathbf{A}_L \frac{\partial \boldsymbol{\Phi}(s_m)}{\partial s_m} x_{mL})^{\mathrm{T}}]^{\mathrm{T}}
\end{aligned} \tag{38}$$

$$\begin{aligned}
\frac{\partial \mathbf{C}(\boldsymbol{\xi})}{\partial \sigma_{\mathrm{w}}^2} &= \mathbf{I}_L \otimes \mathbf{R}_{\hat{\mathrm{w}}} \\
\frac{\partial \mathbf{C}(\boldsymbol{\xi})}{\partial c_{mn}} &= \sigma_{\mathrm{w}}^2 \mathbf{I}_L \otimes \frac{\partial \mathbf{R}_{\hat{\mathrm{w}}}}{\partial c_{mn}} \\
\frac{\partial \mathbf{C}(\boldsymbol{\xi})}{\partial |x_{ml}|} &= \mathbf{0}_{KL\times KL} \\
\frac{\partial \mathbf{C}(\boldsymbol{\xi})}{\partial \phi_{ml}} &= \mathbf{0}_{KL\times KL} \\
\frac{\partial \mathbf{C}(\boldsymbol{\xi})}{\partial s_m} &= \mathbf{0}_{KL\times KL}
\end{aligned} \tag{39}$$

where $\otimes$ is the Kronecker product, and $\mathbf{0}_{m\times n}$ denotes the $m \times n$ all-zero matrix, and $\frac{\partial \boldsymbol{\Phi}(s_p)}{\partial s_p}$ represents the derivative of $\boldsymbol{\Phi}(s_p)$ with respect to s_p, which can be easily obtained.

B. Random Parameters

The derivatives of mean $\boldsymbol{\mu}(\boldsymbol{\xi})$ and covariance $\mathbf{C}(\boldsymbol{\xi})$ with respect to $\boldsymbol{\xi}_{\boldsymbol{r}}$ can be derived as

$$\frac{\partial \boldsymbol{\mu}(\boldsymbol{\xi})}{\partial \theta_{ml}} = [\mathbf{0}_{K\times 1}^{\mathrm{T}} \cdots (\frac{\partial \mathbf{A}_l}{\partial \theta_{ml}} \boldsymbol{\Phi} \mathbf{x}_l)^{\mathrm{T}} \cdots \mathbf{0}_{K\times 1}^{\mathrm{T}}]^{\mathrm{T}} \tag{40}$$

$$\frac{\partial \mathbf{C}(\boldsymbol{\xi})}{\partial \theta_{ml}} = \mathbf{0}_{KL\times KL} \tag{41}$$

C. Expectation Calculation on Random Parameters

After the calculation of partial derivatives of $\boldsymbol{\mu}(\boldsymbol{\xi})$ and $\mathbf{C}(\boldsymbol{\xi})$ with respect to parameters $\boldsymbol{\xi}$ (refer to the Equations (38) (39) (40) and (41)), the expectation with respect to random variables are given by the following equations

$$\begin{aligned}
\mathbf{E}_{\boldsymbol{\xi}_{\boldsymbol{r}}} \left(\mathbf{A}_l^{\mathrm{H}} {\mathbf{R}_{\hat{\mathrm{w}}}}^{-1} \mathbf{A}_l \right) &= \mathbf{R}_{\mathbf{a}} \odot {\mathbf{R}_{\hat{\mathrm{w}}}}^{-1} \\
\mathbf{E}_{\boldsymbol{\xi}_{\boldsymbol{r}}} \left(\mathbf{A}_l^{\mathrm{H}} {\mathbf{R}_{\hat{\mathrm{w}}}}^{-1} \frac{\partial \mathbf{A}_l}{\partial \theta_{kl}} \right) &= j[\mathbf{R}_{\mathbf{a}} \odot {\mathbf{R}_{\hat{\mathrm{w}}}}^{-1}] \mathbf{O}_{kk} \\
\mathbf{E}_{\boldsymbol{\xi}_{\boldsymbol{r}}} \left(\frac{\partial \mathbf{A}_l^{\mathrm{H}}}{\partial \theta_{kl}} {\mathbf{R}_{\hat{\mathrm{w}}}}^{-1} \frac{\partial \mathbf{A}_l}{\partial \theta_{il}} \right) &= \mathbf{O}_{kk}[\mathbf{R}_{\mathbf{a}} \odot {\mathbf{R}_{\hat{\mathrm{w}}}}^{-1}] \mathbf{O}_{ii} \\
\mathbf{E}_{\boldsymbol{\xi}_{\boldsymbol{r}}} \left[\frac{\partial^2}{\partial \theta_{kl} \partial \theta_{il}} \left(\frac{\boldsymbol{\theta}_l^{\mathrm{T}} \mathbf{C}_\theta^{-1} \boldsymbol{\theta}_l}{2\sigma_\theta^2} \right) \right] &= \frac{\rho_{ki}^{'}}{\sigma_\theta^2}
\end{aligned} \tag{42}$$

where $\mathbf{O}_{ki}$ denotes that the element at the k-th row and i-th column of the matrix is 1, while the others are 0, and $\rho_{ki}^{'}$ is the k-th row and i-th column element of the inverse matrix of $\mathbf{C}_\theta$.

ACKNOWLEDGMENT

The authors would like to thank the anonymous reviewers for their insightful comments, which have helped the authors improve the quality of this paper significantly.

REFERENCES

[1] G. Fornaro, F. Lombardini, A. Pauciullo, D. Reale, and F. Viviani, "Tomographic Processing of Interferometric SAR Data: Developments, applications, and future research perspectives," *IEEE Signal Processing Magazine*, vol. 31, pp. 41-50, 2014.

[2] A. Reigber and A. Moreira, "First demonstration of airborne SAR tomography using multibaseline L-band data," *IEEE Transactions on Geoscience and Remote Sensing*, vol. 38, pp. 2142-2152, 2000.

[3] G. Fornaro, F. Serafino, and F. Soldovieri, "Three-dimensional focusing with multipass SAR data," *IEEE Transactions on Geoscience and Remote Sensing*, vol. 41, pp. 507-517, 2003.

[4] G. Fornaro, F. Lombardini, and F. Serafino, "Three-dimensional multipass SAR focusing: experiments with long-term spaceborne data," *IEEE Transactions on Geoscience and Remote Sensing*, vol. 43, pp. 702-714, 2005.

[5] G. Fornaro and F. Serafino, "Imaging of Single and Double Scatterers in Urban Areas via SAR Tomography," *IEEE Transactions on Geoscience and Remote Sensing*, vol. 44, pp. 3497-3505, 2006.

[6] X. X. Zhu and R. Bamler, "Tomographic SAR Inversion by L1−Norm Regularization −− The Compressive Sensing Approach," *IEEE Transactions on Geoscience and Remote Sensing*, vol. 48, pp. 3839-3846, 2010.

[7] X. X. Zhu and R. Bamler, "Very High Resolution Spaceborne SAR Tomography in Urban Environment," *IEEE Transactions on Geoscience and Remote Sensing*, vol. 48, pp. 4296-4308, 2010.

[8] X. X. Zhu and R. Bamler, "Super-Resolution Power and Robustness of Compressive Sensing for Spectral Estimation With Application to Spaceborne Tomographic SAR," *IEEE Transactions on Geoscience and Remote Sensing*, vol. 50, pp. 247-258, 2012.

[9] X. X. Zhu and R. Bamler, "Demonstration of Super-Resolution for Tomographic SAR Imaging in Urban Environment," *IEEE Transactions on Geoscience and Remote Sensing*, vol. 50, pp. 3150-3157, 2012.

[10] Y. Y. Wang, X. X. Zhu and R. Bamler, "An Efficient Tomographic Inversion Approach for Urban Mapping Using Meter Resolution SAR Image Stacks," *IEEE Geoscience and Remote Sensing Letters*, vol. 11, pp. 1250-1254, 2014.

[11] X. X. Zhu and R. Bamler, "Superresolving SAR Tomography for Multidimensional Imaging of Urban Areas: Compressive sensing-based TomoSAR inversion," *IEEE Signal Processing Magazine*, vol. 31, pp. 51-58, 2014.

[12] A. Budillon, A. Evangelista, and G. Schirinzi, "Three-Dimensional SAR Focusing From Multipass Signals Using Compressive Sampling," *IEEE Geoscience and Remote Sensing Letters*, vol. 49, pp. 488-499, 2011.

[13] X. Sun, A. Yu, Z. Dong, and D. Liang, "Three-Dimensional SAR Focusing via Compressive Sensing: The Case Study of Angel Stadium," *IEEE Geoscience and Remote Sensing Letters*, vol. 9, pp. 759-763, 2012.

[14] M. Schmitt and U. Stilla, "Layover separation in airborne single pass multi-baseline InSAR data based on compressive sensing," in *Proc. EUSAR*, pp. 30-33, 2012.

[15] M. Schmitt and U. Stilla, "Compressive Sensing Based Layover Separation in Airborne Single-Pass Multi-Baseline InSAR Data," *IEEE Geoscience and Remote Sensing Letters*, vol. 10, no. 2, pp. 313-317, 2013.

[16] L. Liang, H. Guo, and X. Li, "Three-Dimensional Structural Parameter Inversion of Buildings by Distributed Compressive Sensing-Based Polarimetric SAR Tomography Using a Small Number of Baselines," *IEEE Journal of Selected Topics in Applied Earth Observations and Remote Sensing*, vol. 7, no. 10, pp. 4218-4230, 2014.

[17] X. X. Zhu, G. Nan, and S. Muhanmad, "Joint Sparsity in SAR Tomography for urban Mapping," *IEEE Journal of Selected Topics in Signal Processing*, vol. 9, no. 8, pp. 1498-1509, 2015.

[18] F. Gini, "A radar application of a modified Cramér-Rao bound: parameter estimation in non-Gaussian clutter," *IEEE Transactions on Signal Processing*, vol. 46, pp. 1945-1953, 1998.

[19] P. Tichavsky, C. H. Muravchik, and A. Nehorai, "Posterior Cramér-Rao bounds for discrete-time nonlinear filtering," *IEEE Transactions on Signal Processing*, vol. 46, pp. 1386-1396, 1998.

[20] C. Hue, J. P. L. Cadre, and P. Perez, "Posterior Cramér-Rao bounds for multi-target tracking," *IEEE Transactions on Aerospace and Electronic Systems*, vol. 42, pp. 37-49, 2006.

[21] W. Yiyin, G. Leus, and A. J. v. d. Veen, "Cramér-Rao bound for range estimation," in *IEEE International Conference on Acoustics, Speech and Signal Processing* (ICASSP 2009), 2009, pp. 3301-3304.

[22] A. M. Guarnieri and S. Tebaldini, "Hybrid Cramér-Rao Bounds for Crustal Displacement Field Estimators in SAR Interferometry," *IEEE Signal Processing Letters*, vol. 14, pp. 1012-1015, 2007.

[23] S. Bay, B. Geller, A. Renaux, J. P. Barbot, and J. M. Brossier, "On the Hybrid Cramér Rao Bound and Its Application to Dynamical Phase Estimation," *IEEE Signal Processing Letters*, vol. 15, pp. 453-456, 2008.

[24] K. Todros and J. Tabrikian, "Hybrid lower bound via compression of the sampled CLR function," in *IEEE/SP 15th Workshop on Statistical Signal Processing* (SSP '09), 2009, pp. 602-605.

[25] M. Pardini, F. Lombardini, and F. Gini, "The Hybrid Cramér-Rao Bound on Broadside DOA Estimation of Extended Sources in Presence of Array Errors," *IEEE Transactions on Signal Processing*, vol. 56, pp. 1726-1730, 2008.

[26] R. Prasad and C. R. Murthy, "Cramér-Rao-Type Bounds for Sparse Bayesian Learning," *IEEE Transactions on Signal Processing*, vol. 61, pp. 622-632, 2013.

[27] C. Ren, J. Galy, E. Chaumette, P. Larzabal, and A. Renaux, "Hybrid lower bound on the MSE based on the Barankin and Weiss-Weinstein bounds," in *Proc. of IEEE International Conference on Acoustics, Speech and Signal Processing* (ICASSP 2013), 2013, pp. 5534-5538.

[28] D. Zachariah and P. Stoica, "Cramér-Rao Bound Analog of Bayes' Rule [Lecture Notes]," *IEEE Signal Processing Magazine*, vol. 32, pp. 164-168, 2015.

[29] D. C. Rife and R. R. Boorstyn, "Multiple Tone Parameter Estimation From Discrete-Time Observations," *Bell System Technical Journal*, vol. 55, pp. 1389-1410, 1976.

[30] P. Stoica and R. L. Moses, "Spectral Analysis of Signals," *Prentice Hall*, 2005.

[31] B. Yang and H. Xu, "The Hybrid Cramér-Rao Bounds on Elevation in Compressive Sensing SAR Tomography," *in 4th Int. Workshop on Compressed Sensing on Radar, Sonar, and Remote Sensing* (CoSeRa 2016), pp. 129-133, 2016.

[32] A. Ferretti, C. Prati, and F. Rocca, "Nonlinear subsidence rate estimation using permanent scatterers in differential SAR interferometry," *IEEE Transactions on Geoscience and Remote Sensing*, vol. 38, pp. 2202-2212, 2000.

[33] A. Ferretti, C. Prati, and F. Rocca, "Permanent scatterers in SAR interferometry," *IEEE Transactions on Geoscience and Remote Sensing*, vol. 39, pp. 8-20, 2001.

[34] A. Parizzi and R. Brcic, "Adaptive InSAR Stack Multilooking Exploiting Amplitude Statistics: A Comparison Between Different Techniques and Practical Results," in *IEEE Geoscience and Remote Sensing Letters*, vol. 8, pp. 441-445, 2011.

[35] G. Vasile, E. Trouv, M. Ciuc, and V. Buzuloiu, "General adaptive-neighborhood technique for improving synthetic aperture radar interferometric coherence estimation," *Journal of the Optical Society of America A*, vol. 21, pp. 1455-1464, 2004.

[36] H. A. Zebker, and J. Villasenor, "Decorrelation in Interferometric Radar Echoes," *IEEE Transactions on Geoscience and Remote Sensing*, vol. 30, no. 5, pp. 950-959, 1992.

[37] F. Gini, and F. Lambardini, "Multibaseline Cross-Track SAR Interferometry: A Signal Processing Perspective," *IEEE Aerospace & Electronic Systems Magazine*, vol. 20, no. 8, pp. 71-93, 2005.

[38] F. De Zan, "Optimizing SAR interferometry for decorrelating scatters," Ph.D. dissertation, Politecnico di Milano, Milan, Italy, 2008.

[39] A. Pauciullo, A. D. Maio, S. Perna, D. Reale, and G. Fornaro, "Detection of Partially Coherent Scatterers in Multidimensional SAR Tomography: A Theoretical Study," *IEEE Transactions on Geoscience and Remote Sensing*, vol. 52, no. 12, pp. 7534-7548, 2014.

[40] M. Lucido, F. Meglio, V. Pascazio, and G. Schirinzi, "Closed-Form Evaluation of the Second-Order Statistical Distribution of the Interferometric Phases in Dual-Baseline SAR Systems," *IEEE Transactions on Signal Processing*, vol. 58, no. 3, pp. 1698-1707, 2010.

[41] V. Pascazio and G. Schirinzi, "Multifrequency InSAR height reconstruction through maximum likelihood estimation of local planes parameters," *IEEE Transactions on Image Processing*, vol. 11, no. 12, pp. 1478-1489, 2002.

[42] G. Ferraiuolo, V. Pascazio, and G. Schirinzi, "Maximum a posteriori estimation of height profiles in InSAR imaging," *IEEE Geoscience Remote Sensing Letters*, vol. 1, no. 2, pp. 66-70, 2004.

[43] M. Eineder and N. Adam, "A maximum-likelihood estimator to simultaneously unwrap, geocode, and fuse SAR interferograms from different viewing geometries into one digital elevation model," *IEEE Transactions on Geoscience and Remote Sensing*, vol. 43, no. 1, pp. 24-36, 2005.

[44] C. Oliver, S. Quegan, "Understanding synthetic aperture radar images," *SciTech Publishing*, 2004.

[45] S. M. Kay, "Fundamentals of Statistical Signal Processing," *New Jersey: Prentice Hall*, 1998.

[46] A. D. Maio, G. Fornaro, and A. Pauciullo, "Detection of Single Scatterers in Multidimensional SAR Imaging," *IEEE Transactions on Geoscience and Remote Sensing*, vol. 47, pp. 2284-2297, 2009.

[47] D. Reale, A. Pauciullo, G. Fornaro, and A. D. Maio, "A scatterers detection scheme in SAR Tomography for reconstruction and monitoring of individual buildings," in *Joint Urban Remote Sensing Event* (JURSE), 2011, pp. 249-252.

[48] G. Fornaro, A. Pauciullo, F. Lombardini, and M. Pardini, "Detection of Single and Multiple Scatterers in Multibaseline Multitemporal SAR Data," in *Proc. IEEE International Geoscience and Remote Sensing Symposium* (IGARSS 2008), 2008, pp. II-453-II-456.

[49] A. D. Maio, G. Fornaro, A. Pauciullo, and D. Reale, "Detection of double scatterers in SAR Tomography," in *Proc. IEEE International Geoscience and Remote Sensing Symposium* (IGARSS 2009), 2009, pp. III-172-III-175.

[50] A. Pauciullo, D. Reale, A. D. Maio, and G. Fornaro, "Detection of Double Scatterers in SAR Tomography," *IEEE Transactions on Geoscience and Remote Sensing*, vol. 50, pp. 3567-3586, 2012.

[51] D. Reale, G. Fornaro, A. Pauciullo, X. Zhu, and R. Bamler, "Tomographic Imaging and Monitoring of Buildings With Very High Resolution SAR Data," in *IEEE Geoscience and Remote Sensing Letters*, vol. 8, pp. 661-665, 2011.

[52] C. Wang, G. Wang, Z. Zhu and C. Ke, "Structure Design of Beijing Capital International Airport Terminal 3," *Building Structure*, vol. 38, no. 1, pp. 16-24, 2008.

[53] M. Villano, "SNR and Noise Variance Estimation in Polarimetric SAR Data," *IEEE Geoscience and Remote Sensing Letters*, vol. 11, no. 1, pp. 278-282, 2014.